Turbulent flow symmetry-breaking in periodic porous media in the intermediate porosity flow regime

Vishal Srikanth*, Andrey V Kuznetsov*,§
*Department of Mechanical and Aerospace Engineering, North Carolina State University,
Raleigh, NC 27695

§Correspondence author. Email: avkuznet@ncsu.edu

ABSTRACT In this paper, we report a novel symmetry-breaking phenomenon that occurs in turbulent convective flow in periodic porous media in the intermediate porosity flow regime for values of porosities in between 0.8 and 0.9. Large eddy simulation is used to numerically simulate the momentum and thermal transport inside the porous medium at the microscale level. The phenomenon is observed to occur for periodically repeating porous media consisting of an in-line arrangement of circular cylinder solid obstacles, such as typically found in heat exchangers. The transition from symmetric to asymmetric flow occurs in between the pore scale Reynolds numbers of 37 (laminar) and 100 (turbulent), and asymmetric flow patterns are reported for Reynolds numbers up to 1,000. A Hopf bifurcation resulting in unsteady oscillatory laminar flow marks the origin of a secondary flow instability arising from the interaction of the shear layers around the solid obstacle. In turbulent flow, stochastic phase difference in the vortex wake oscillations caused by the secondary flow instability results in asymmetrical velocity and temperature distributions in the pore space. Consequently, high and low velocity flow channels are formed in the pore space that leads to the asymmetrical velocity and pressure distributions. At the macroscale level, symmetry-breaking results in residual transverse drag force components acting on the solid obstacle surfaces. The vortex wake oscillations caused by the secondary flow instability promote attached flow on the solid obstacle surface, which improves the surface averaged heat flux from the solid obstacle surface.

INTRODUCTION

Turbulence in porous media emerges for pore-scale Reynolds number values that are of the order of 100 [Seguin *et al.* 1998]. Turbulent flow is encountered in a wide range of flow scenarios such as the flow through industrial scale heat exchangers [Nield & Bejan 2017], cooling systems for electronics [Zhao & Lu 2002], and forest fire modeling [Mell *et al.* 2009]. The solid obstacles that compose the porous medium in the above flow scenarios are often cylindrical in shape and the space between them is close enough that the vortices that are formed behind the solid obstacles impinge on the neighboring solid obstacle that is located downstream. Understanding the characteristics of turbulent flow in porous media and developing robust turbulence models is crucial to model naturally occurring porous media such as forests. More importantly, it will enable targeted engineering of the next-generation porous materials whose microscale geometries produce optimal thermal performance.

Previous studies that focused on flow in periodic porous media have shown the turbulence length and time scale limitations imposed by the pore geometry [Chu et al. 2018; He et al. 2018, 2019; Nguyen et al. 2019; Uth et al. 2016] and suggested the absence of macroscale turbulent structures [Jin et al. 2015; Jin & Kuznetsov 2017]. It is noted that macroscale turbulence may survive at very high porosity (>98%) [Rao & Jin 2022], but the result must be confirmed for large simulation domains. Turbulent flow structures are generated as microscale vortices behind the solid obstacles that compose the porous medium [Srikanth et al. 2021]. The turbulent structures are then advected downstream where they are dissipated under the action of shear and pressure gradients. Therefore, the properties of microscale turbulence and the

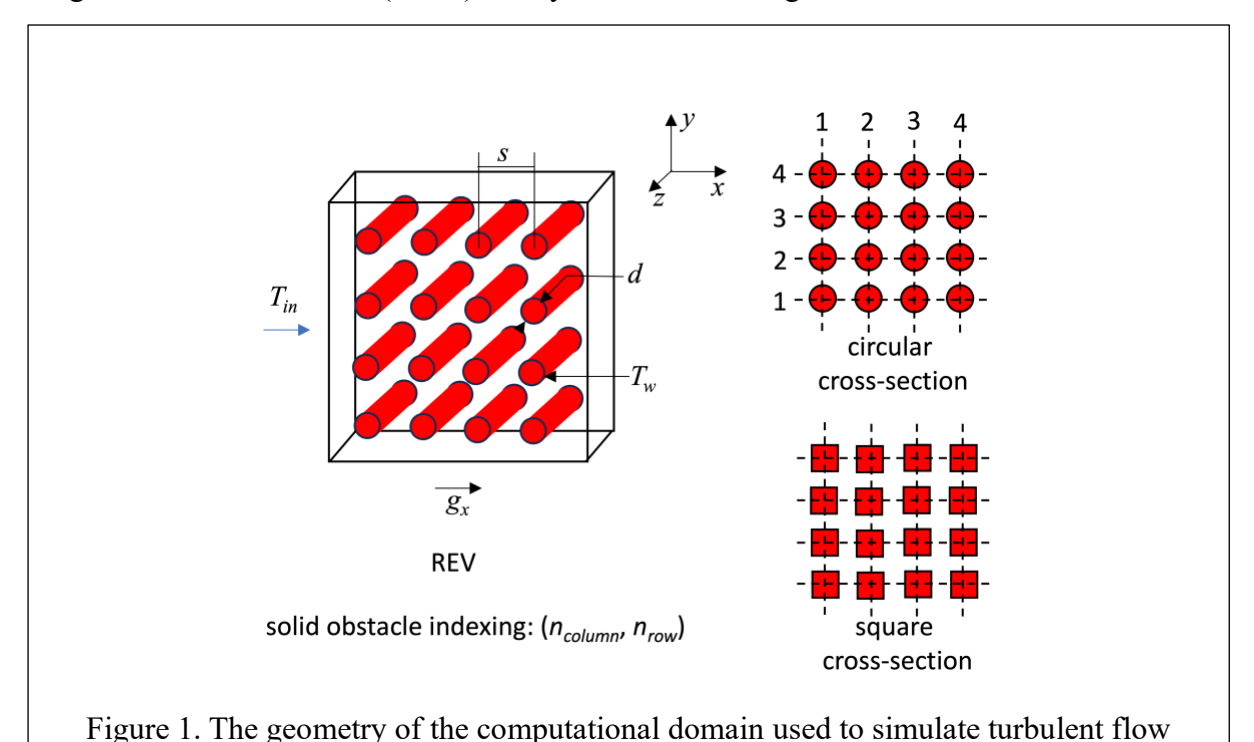
related macroscale flow variables such as drag and heat flux are determined by the distribution of shearing and recirculating flow regions inside the pores. These observations have been reported for a wide range of geometries and Reynolds numbers in [Chu et al. 2018; He et al. 2019; Huang et al. 2022; Srikanth et al. 2021]. We note that there is a strong dependence of the turbulent flow distribution on the solid obstacle surface with the geometry of the porous medium.

In this paper, we divide turbulent flow in porous media into three flow regimes with respect to the porosity (φ): low, intermediate, and high porosity flow regimes. At low porosity (φ <0.8), the surfaces of the solid obstacles are close to each other such that the pore spaces are equivalent to a network of interconnected channels. Recirculating microscale vortices are formed behind the solid obstacles for low porosity and their size is limited by the pore space. Flow symmetry-breaking has been observed in the low porosity regime due to the formation of an adverse pressure region in the pore space [Srikanth et al. 2021]. In the present study, we investigate a novel symmetry-breaking phenomenon that occurs in the intermediate porosity flow regime (0.8< φ <0.95) for cylindrical solid obstacles with circular cross-section. At intermediate porosity, the diameter of the microscale vortices that are formed behind the circular cylinders is approximately equal to the radius of the cylinder and smaller than the pore size by at least a factor of 2. There is adequate pore space in between the solid obstacles in the intermediate porosity regime to allow the development of shedding vortices. However, the vortices interact with the neighboring solid obstacles at a downstream location resulting in complex flow phenomena and flow instabilities that we discuss in this paper. We note that at high porosity (φ >0.95), the large pore space in between the solid obstacles results in the independence of the flow patterns surrounding the solid obstacle with respect to its neighbor.

NUMERICAL METHOD

In this paper, we are investigating turbulent flow inside a periodic porous medium composed of cylindrical solid obstacles (Figure 1). The cylindrical obstacles that have circular and square cross-sections are placed in an in-line arrangement separated by a distance, s, which we are calling the pore size. We numerically simulate the turbulent flow inside the pores at the microscale level by using Large Eddy Simulation (LES). We model a Representative Elementary Volume (REV) of the porous medium consisting of 4x4 arrangement of solid obstacles (Dimensions - 4s x4s x 2s). We apply periodic boundary conditions at all of the boundaries of the REV. We sustain flow at a constant pore scale Reynolds number (Re) by applying a momentum source term g_i . The Reynolds number is calculated using the hydraulic diameter of the solid obstacle, d, and the double averaged (time and space) x- velocity, u_m . The governing equations of momentum are non-dimensionalized by setting the fluid density, d, and u_m equal to 1 and the dynamic viscosity equal to 1/Re. The governing equation of thermal energy is solved as a passive scalar in the dimensional form. The material properties of water are used for the thermal energy equation, where specific heat capacity c_p is 4182 J/KgK and thermal conductivity k = 0.6 W/mK. We have set the bulk inlet temperature (T_{in}) equal to 323K and the wall temperature (T_w) equal to 353K.

We use ANSYS Fluent 16.0 to solve the governing equations for LES with the Dynamic One-equation Turbulence Kinetic Energy (DOTKE) subgrid scale model by applying the finite volume method. The governing equations and details of the model implementation are available in [ANSYS Inc. 2016] and in our previous work [Huang *et al.* 2022; Srikanth *et al.* 2021] along with validation studies for the momentum and thermal transport models and convergence of the grid and REV sizes. We demonstrated that LES with DOTKE subgrid scale modeling reproduces the experimentally measured pressure and Nusselt number distributions on the surface of tubes in an in-line tube bank [Aiba *et al.* 1982]. We have also demonstrated that a grid resolution of $\Delta x/s = 0.02$ is sufficient to resolve a substantial portion of the turbulence kinetic energy (volume averaged LES index of quality [Celik *et al.* 2005] = 0.95) until the magnitude of turbulence kinetic energy declines by 3 orders of magnitude at the smallest resolved length scale when compared to the large scale eddies. Stretched grid cells of size $\Delta y/s = 0.001$ are used near the solid obstacle walls to resolve the near-wall boundary layer accurately. The maximum value of $\Delta y^+ = 1.5$ and the grid cell growth rate is 1.2, which places \sim 3 grid cells in the laminar (linear) sublayer even for the regions with the maximum shear.



We use bounded second order central differencing discretization for the convective terms and second order central differencing discretization for the diffusive terms of the momentum equation. We use the QUICK scheme for the convective term of the thermal energy equation. We solve the momentum and pressure Poisson equations in a segregated manner using the PISO algorithm [Issa 1986]. We solve the thermal energy equation at the end of the time step. We advance the simulation in time by using a second order (implicit) backward Euler method. The simulations span 400 non-dimensional time units (17,000 CPU-Hours) to converge the turbulence statistics, which corresponds to 200 flow-through cycles for a unit cell. We have

confirmed that the modes of symmetry-breaking reported in the paper are not caused by

inside the REV of the porous medium.

unconverged turbulence statistics by verifying that the same modes are observed over 2 different time intervals.

RESULTS AND DISCUSSION

Secondary flow instabilities and symmetry-breaking phenomena in porous media are sensitive to two key parameters: porosity and Reynolds number, and symmetry-breaking is often conditional on the smoothness of the solid obstacle surface. A case study of the variation of porosity is used to characterize the novel symmetry-breaking phenomenon that occurs in the intermediate porosity flow regime. We report the effect that the asymmetrical flow pattern has on turbulent convection heat transfer.

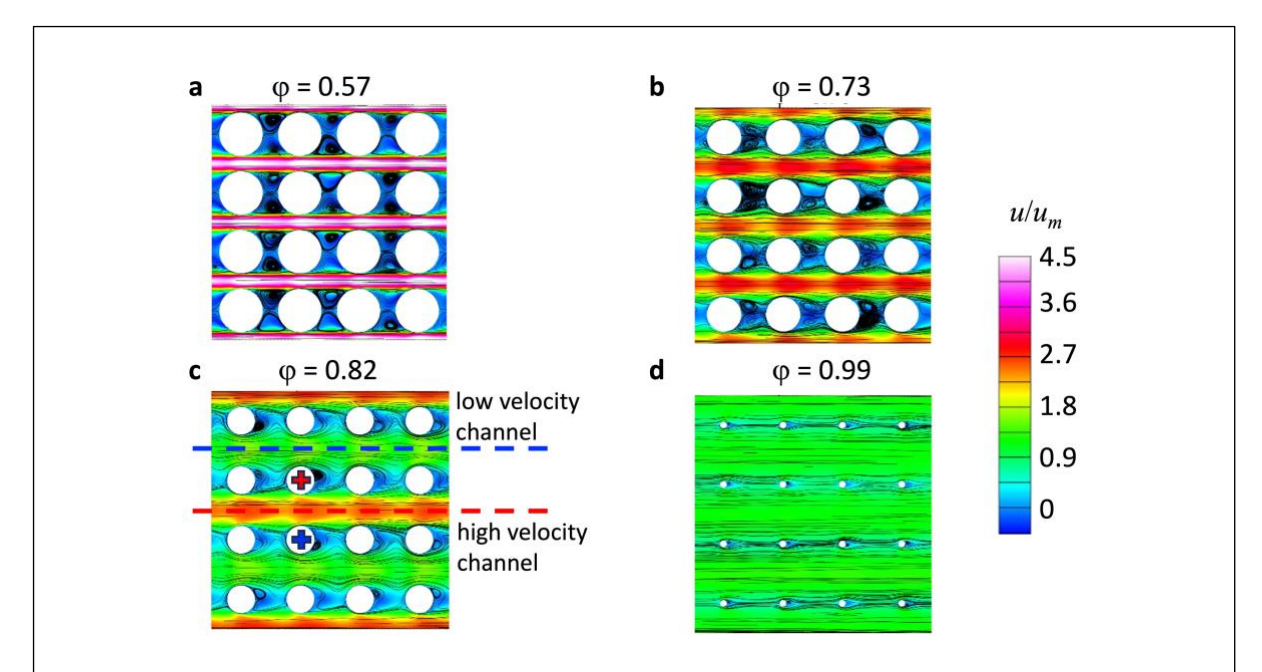


Figure 2. Reynolds averaged flow streamlines plotted for different values of porosity shows that symmetry-breaking occurs for $\varphi = 0.82$ (intermediate porosity) at Re = 300. The colors show the Reynolds averaged x- velocity distribution.

Turbulent flow in porous media breaks symmetry in both the low and intermediate porosity flow regimes. Symmetry-breaking occurs due to the interaction of the flow around a solid obstacle with the neighboring solid obstacle. Therefore, the distance between the solid obstacle surfaces, which is determined by the porosity, is the primary variable that controls the occurrence of symmetry-breaking. Consider turbulent flow at a Reynolds number of 300 inside a periodic porous medium consisting of cylindrical solid obstacles with circular cross-section. In the low porosity flow regime ($\varphi < 0.8$), a secondary flow instability is formed due to competing pressure and inertial force components in the confined pore space, which drives the flow to break symmetry. A pair of shear layers form around the solid obstacle surface starting in the location where the flow separates (Figure 2(a) and (b)). The secondary flow instability at low porosity is characterized by the Kelvin-Helmholtz instability since the pair of shear layers do not interact due to the confined pore space and the von Karman instability cannot be formed (until symmetry is broken). Symmetry-breaking at low porosity manifests above a critical Reynolds number (Re = 350-500) with deviatory flow streamlines resulting in a change in the direction of the macroscale flow at an angle that is determined by the value of porosity.

The symmetry-breaking phenomenon at low porosity is described in detail in our previous work [Srikanth *et al.* 2021]. We noted that deviatory flow terminates at $\varphi = 0.8$ and demarcates the transition between the low and intermediate porosity flow regimes.

For turbulent flow at Re = 300 in the intermediate porosity flow regime (0.8 < φ < 0.95), the pair of shear layers that are formed around the solid obstacle surface interact with one another in a manner that is similar to von Karman vortex shedding (Figure 2(c)). Interaction between the shear layers is possible at intermediate values of porosity by the presence of an adequate separation distance between the solid obstacle surfaces. However, unlike in the case of external flow around a single isolated solid obstacle, the interaction of the shear layers and subsequent formation of the von Karman vortex street is influenced by the presence of the neighboring solid obstacles downstream of the vortex wake. The result is a new type of instability that combines the von Karman vortex shedding and a secondary flow instability. The occurrence of the traditional von Karman vortex shedding behind the solid obstacle is hindered by the possibility that the vortices will immediately impinge on the downstream solid obstacle. A secondary flow instability occurs to divert the path of the shedding vortices such that it circumnavigates the solid obstacle into the pore space without directly impinging on the solid obstacle surface. Thus, the von Karman vortex shedding is superimposed on the oscillations of the secondary flow instability such that vortices are shed into the pore space above and below the solid obstacle in an alternating manner (Figure 3). We note that this secondary flow instability is not observed in the high porosity flow regime due to the large separation distance between the adjacent solid obstacle surfaces (Figure 2(d)).

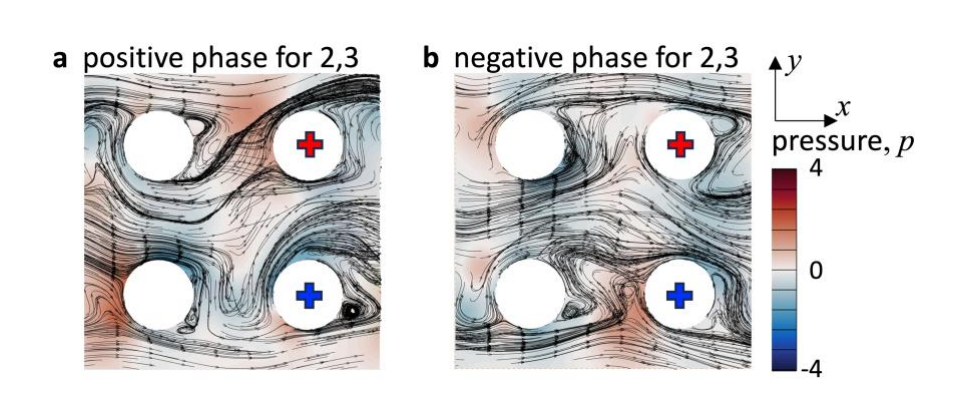


Figure 3. Instantaneous flow streamlines plotted at 2 different time steps (a and b) separated by 28 non-dimensional time units show the oscillations of the secondary flow instability that causes vortex shedding to alternate between the pore space above and below the solid obstacles. The colors show the instantaneous pressure distribution.

In the present case where the solid obstacle cross-section is circular, the secondary flow instability introduces an oscillatory shift in the stagnation and separation points on the solid obstacle surface (Figure 3). Consider the path of the vortex shedding behind the solid obstacle on the top right location in Figure 3 (marked with a red plus). In Figure 3(a), the vortex shedding path is tilted in the positive *y*- direction (positive phase) such that the separated flow region on the solid obstacle surface occupies the top-right quadrant. Note that a separation bubble is formed in the bottom-right quadrant, which is followed by flow reattachment on the solid obstacle surface. Correspondingly, the stagnation point is located in the bottom-left quadrant of the solid obstacle surface. When the oscillation caused by the secondary flow

instability proceeds in time (Figure 3(b)), the locations of the separated flow region and the stagnation point on the solid obstacle surfaces are mirrored when compared to Figure 3(a) (negative phase). It is evident from the streamline plots in Figure 3 that the oscillatory behavior of the secondary flow instability introduces a shift in the separation and stagnation points along the solid obstacle surfaces and increases the fraction of the solid obstacle surface that is occupied by the attached flow regions when compared to the separated flow regions.

When the instantaneous flow distribution is Reynolds averaged, the Reynolds averaged velocity (Figure 2(c)) and pressure distributions exhibit a lack of symmetry. The Reynolds averaged velocity distribution consists of alternating high and low velocity channels in the transverse direction that is perpendicular to the direction of the applied pressure gradient (g_x) . Here, the term channel refers to the pore space in between the solid obstacles oriented along the direction of the flow (red and blue dashed lines in Figure 2(c) correspond to high and low velocity channels). Close examination of the Reynolds averaged flow streamlines in Figure 2(c) also reveal asymmetrical recirculation regions as well as an offset in the stagnation point with respect to the geometric plane of symmetry. In the present flow setup, the geometric plane of symmetry that we are referring to is one that bisects the solid obstacle cross-section and is oriented parallel to the xz- plane. This type of symmetry-breaking occurs only in the intermediate porosity flow regime when the oscillatory vortex shedding path emerges due to the secondary flow instability.

These high and low velocity channels can also be observed in the experimentally measured mean streamwise velocity profile across a porous medium composed of circular tubes [Kim *et al.* 2023]. The experimental setup of Kim *et al.* [2023] is different when compared to the simulation domain used in the present work. The experiment considers a partially porous channel geometry, whereas the present work considers a fully periodic domain. We also note that the porosity of the porous medium used in the experiment is 0.75, which is in the low porosity flow regime as per the definition used in the present work. However, we note that a porosity of 0.75 is close to the boundary between the low and intermediate porosity flow regimes (separated at $\varphi = 0.8$). The velocity profile measurements for $\varphi = 0.75$ [Kim *et al.* 2023] reveal that the centerline velocity in the pore space changes by 15.1% from the low velocity channel to the high velocity channel (Figure 4(a)), indicating that it may be feasible to observe symmetry-breaking experimentally. Similarly, the velocity profile simulated in the present work for $\varphi = 0.82$ has a 25.3% change in the centerline velocity from the low velocity channel to the high velocity channel (Figure 4(b)).

Note that the magnitudes of the dimensionless x- velocity are different for the simulation and the experiment such that the simulated dimensionless x- velocity is almost twice the experimentally observed dimensionless x- velocity in the velocity channel. For the simulation, the x- velocity is non-dimensionalized with respect to the double averaged (space and time) x- velocity in the periodic REV. For the experiment, the x- velocity is non-dimensionalized with respect to the inlet velocity of the wind tunnel section. Additionally, only a portion of the wind tunnel width is occupied by solid obstacles and the remaining portion is a clear fluid region. With the available information about the experimental setup and velocity distribution, it was not possible to non-dimensionalize both the simulation and experiment with respect to the same characteristic velocity. Therefore, we only present a qualitative comparison of the formation of high and low velocity channels due to the asymmetrical flow distribution.

Unlike the deviatory flow symmetry-breaking that occurs at low porosity, symmetry-breaking at intermediate porosity is not apparent in the instantaneous flow distribution. The high and low velocity cells develop inside the pores when the flow is averaged over time due to asymmetrical oscillations of the vortex shedding path caused by the secondary flow instability. Low velocity cells are formed inside the pores where the vortex shedding duration is longer, whereas high velocity cells are formed in the pores where the vortex shedding duration is shorter. The vortex shedding duration is visualized in the present work by calculating the *y*-pressure force that is acting on the surface of the solid obstacle (Figure 5). If the flow is symmetric, the Reynolds average of the *y*- pressure drag will be equal to zero. In the present case, there exists a bias in the *y*- pressure drag that acts in either the positive or negative *y*-direction depending on the offset location of the stagnation point. Positive bias in the *y*-pressure drag is caused because the duration of the positive phase of the vortex shedding process is greater than the duration of the negative phase (solid obstacle (2,3) in Figure 5). The

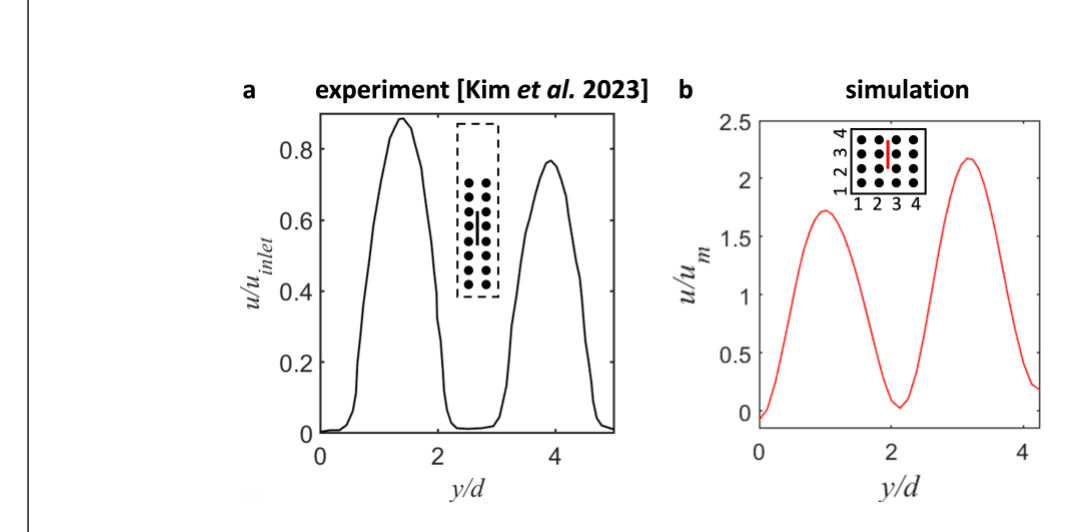


Figure 4. x- velocity profiles (a) measured in Kim et al. [2023] and (b) simulated in the present work in the direction perpendicular to the streamwise direction. The velocity profile shows the formation of high and low velocity channels in the pore space caused by the symmetry-breaking phenomenon. The black and red lines in the sketches show the location of the velocity profile.

asymmetry in the vortex shedding over time is also inferred from the shape of the plot of y-pressure drag in Figure 5. Positive bias in the y- pressure drag for the solid obstacle results in

a low velocity cell in the pores above the solid obstacle. The vice-versa is observed for the solid obstacles with negative bias in the *y*- pressure drag.

We note that the shift in the separation point and the oscillation of the separated flow region on the solid obstacle surface is less intense for cylindrical solid obstacles with square cross-section even though the porosity is the same as the case with circular solid obstacle cross-section. The vertices of the square geometry prescribe the location of the separation points and limit the oscillation of the vortex shedding path. As a result, vortices shed behind square solid obstacles impinge on the adjacent solid obstacles that are downstream, unlike for circular solid obstacles. The size of the vortex structures as well as the fraction of the solid obstacle surface area occupied by separated flow is larger for square solid obstacles when compared to the circular solid obstacles.

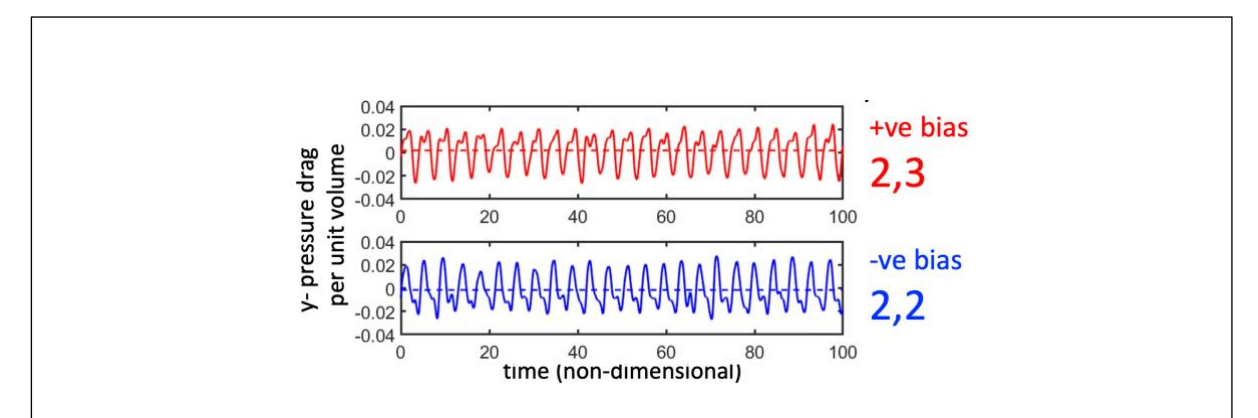


Figure 5. The time series of *y*- pressure drag force acting on the solid obstacle surface showing the bias in the duration of the vortex shedding phases that ultimately results in asymmetrical Reynolds averaged velocity and pressure distributions. The dashed lines show the Reynolds averaged *y*- pressure drag value for the solid obstacle. The locations of the solid obstacles (2,2 and 2,3) are shown in Figure 1.

Symmetry-breaking for flow around cylindrical solid obstacles with circular cross-section is characterized by the occurrence of the secondary flow instability and an oscillatory vortex wake path resulting in attached flow on the solid obstacle surface. These conditions are beneficial to increase the heat flux from the solid obstacle surface to the surrounding fluid. Attached flow on the solid obstacle surface decreases the thermal boundary layer thickness when compared to separated flow, which in turn increases the heat flux from the solid obstacle surface in that region. Additionally, smaller vortices are formed behind the solid obstacles with circular crosssection due to the shift in the separation point caused by the secondary flow instability. There are two factors that cause the improvement of heat transfer from the solid obstacle surface in porous media: (1) small size of the microscale vortices results in a smaller fraction of the solid obstacle surface area covered by recirculating flow and increases local heat flux, and (2) frequent vortex shedding from the solid obstacle surface advects recirculating vortex structures with high core temperature and increases local heat flux. The flow around solid obstacles with circular cross-section combines both of these factors and results in higher surface-averaged heat flux when compared to the solid obstacles with square cross-section. This is further supported by the occurrence of a lower vortex core temperature for solid obstacles with circular cross-section when compared to square cross-section (Figure 6(a)). The core temperature of the vortex increases due to recirculation, but the vortex is subsequently advected during the

rapid vortex shedding process. Therefore, the secondary flow instability that is observed for flow around solid obstacles with circular cross-section promotes heat transfer in porous media in the intermediate porosity regime. When the heat transfer rate is compared for solid obstacles with circular and square cross-section (at $\varphi = 0.87$, Re = 300), the circular solid obstacles have 5% greater double averaged heat flux (and 7% lesser coefficient of drag) when compared to square solid obstacles.

When the temperature distribution is Reynolds averaged in the case of solid obstacles with circular cross-section, symmetry-breaking in the velocity distribution causes asymmetry in the Reynolds averaged temperature distribution (Figure 6(b)). Consequently, the distribution of the Reynolds averaged heat flux on the solid obstacle surface is asymmetrical (Figure 6(c)). The

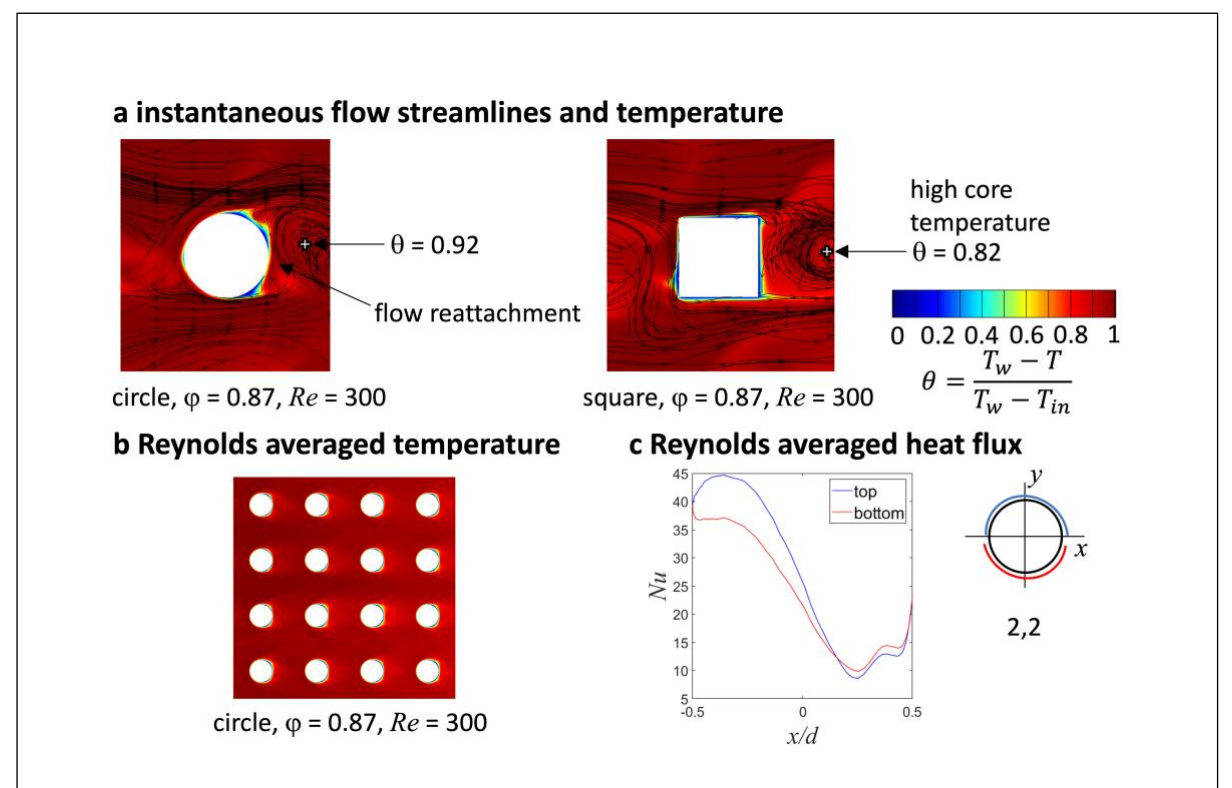


Figure 6. (a) the instantaneous temperature distribution around solid obstacle (2,2) reveals that vortex structures are smaller and have lower core temperature for circular cross-section when compared to square cross-section. (b) The effect of symmetry breaking on the Reynolds averaged temperature distribution is not as prominent as the velocity distribution. (c) Symmetry-breaking causes asymmetric Nusselt number distribution on the solid obstacle surface.

heat flux has a higher magnitude on the surface of the solid obstacle that is exposed to the high velocity channel when compared to the low velocity channel. However, this asymmetry does not appear to have any effect on the double averaged Nusselt number over the entire REV since the increase in the solid obstacle surface heat flux caused by the high velocity channel is counterbalanced by the decrease in the heat flux caused by the low velocity channel.

In this paper, we identified three flow regimes for turbulent flow in porous media with respect to the porosity: low, intermediate, and high porosity flow regimes. The regimes were based on the behavior of the microscale vortex structures for different porosities. We expect the porosity values at which the different flow regimes change to increase with the increase in the Reynolds number. We simulated turbulent convection heat transfer in the intermediate porosity regime $(0.8 < \phi < 0.95)$ for porous media composed of cylindrical solid obstacles, such as typically found in heat exchangers. In the intermediate porosity flow regime, we investigated a novel secondary flow instability and a symmetry-breaking phenomenon, which have a significant influence on the microscale velocity distribution and the heat transfer from the solid obstacle surface to the surrounding flow.

The secondary flow instability was found to be caused by the interaction of the shear layers that are formed around the solid obstacle surface during the formation of the von Karman instability. The microscale vortices that are formed behind the solid obstacles are in the proximity of the neighboring solid obstacle that is at a downstream location. This causes the secondary flow instability where the vortex wake behind the solid obstacle starts oscillating around the downstream solid obstacle and advecting vortex structures into the pore space rather than impinging on the solid obstacle surface. The resulting flow pattern surrounding the solid obstacle surface consists of more surface area covered by attached flow due to a shift in the separation point that is caused by the vortex wake oscillations. We note that the oscillatory vortex wake does not occur for cylindrical solid obstacles with square cross-section since the vertices of the square geometry prevent the shift in the separation point. Attached flow on the solid obstacle surface and small vortex structures caused by the secondary flow instability result in greater double averaged heat flux on the solid obstacle surface and lower vortex core temperature for solid obstacles with circular cross-section when compared to square cross-section.

The vortex wake oscillations caused by the secondary flow instability are not symmetric with respect to time where either the positive phase of the oscillation spans a greater duration than the negative phase, or vice versa. When the instantaneous flow and temperature distributions caused by the secondary flow instability are averaged over time, the Reynolds averaged velocity and temperature distributions are asymmetric. The asymmetry is more prominent for the velocity distribution leading to the formation of high and low velocity channels in the pore space. Asymmetry in the vortex wake oscillations results in vortices being preferentially advected into a particular pore space, which leads to the formation of a low velocity channel when the flow is averaged over time. Asymmetry is also observed in the distribution of the heat flux on the solid obstacle surface where the solid obstacle surface exposed to the high velocity channel experiences higher heat flux from the solid obstacle surface to the surrounding fluid. However, the increase in the heat flux caused by the high velocity channel is counterbalanced by the decrease in the heat flux by the low velocity channel. Therefore, the heat transfer enhancement for circular solid obstacles compared to square solid obstacles is derived from the effect of the secondary flow instability and the asymmetrical Reynolds averaged heat flux distribution is merely a consequence of the oscillatory wake path.

ACKNOWLEDGEMENTS

The authors acknowledge the computing resources provided by North Carolina State University High Performance Computing Services Core Facility (RRID:SCR_022168). This research was funded by the National Science Foundation award CBET-2042834.

NOMENCLATURE

Quantity	Symbol	Units
Porosity	φ	-
Pore size	S	-
Hydraulic diameter of the	d	-
solid obstacle		
Applied pressure gradient	g_i	-
Double averaged <i>x</i> - velocity	u_m	-
Maximum grid cell size	Δx	m
Near-wall grid cell size	Δy	m
Near-wall grid cell size in	Δy^+	-
wall coordinates		

REFERENCES

- Aiba, S., Tsuchida, H., & Ota, T. [1982]. Heat Transfer Around Tubes in In-line Tube Banks. *Bulletin of JSME*, 25[204], 919–926.
- ANSYS Inc. [2016]. Ansys (R) Academic Research Fluent, Release 16.0, Help System, Fluent Theory Guide.
- Celik, I. B., Cehreli, Z. N., & Yavuz, I. [2005]. Index of resolution quality for large eddy simulations. In *Journal of Fluids Engineering, Transactions of the ASME*. doi:10.1115/1.1990201
- Chu, X., Weigand, B., & Vaikuntanathan, V. [2018]. Flow turbulence topology in regular porous media: From macroscopic to microscopic scale with direct numerical simulation. *Physics of Fluids*, 30[6], 065102.
- He, X., Apte, S., Schneider, K., & Kadoch, B. [2018]. Angular multiscale statistics of turbulence in a porous bed. *Physical Review Fluids*, 3[8], 084501.
- He, X., Apte, S. V., Finn, J. R., & Wood, B. D. [2019]. Characteristics of turbulence in a face-centred cubic porous unit cell. *Journal of Fluid Mechanics*, 873, 608–645.
- Huang, C.-W., Srikanth, V., & Kuznetsov, A. V. [2022]. The evolution of turbulent microvortices and their effect on convection heat transfer in porous media. *Journal of Fluid Mechanics*, 942, A16.
- Issa, R. I. [1986]. Solution of the implicitly discretised fluid flow equations by operator-splitting. *Journal of Computational Physics*, 62[1], 40–65.
- Jin, Y., & Kuznetsov, A. V. [2017]. Turbulence modeling for flows in wall bounded porous media: An analysis based on direct numerical simulations. *Physics of Fluids*, 29[4], 045102.
- Jin, Y., Uth, M. F., Kuznetsov, A. V., & Herwig, H. [2015]. Numerical investigation of the possibility of macroscopic turbulence in porous media: A direct numerical simulation study. *Journal of Fluid Mechanics*, 766, 76–103.
- Kim, J. S., Kang, P. K., He, S., ... Seo, I. W. [2023]. Pore-Scale Flow Effects on Solute Transport in Turbulent Channel Flows Over Porous Media. *Transport in Porous Media*, 146[1], 223–248.
- Mell, W., Maranghides, A., McDermott, R., & Manzello, S. L. [2009]. Numerical simulation and experiments of burning douglas fir trees. *Combustion and Flame*. doi:10.1016/j.combustflame.2009.06.015
- Nguyen, T., Muyshondt, R., Hassan, Y. A., & Anand, N. K. [2019]. Experimental investigation of cross flow mixing in a randomly packed bed and streamwise vortex characteristics using particle image velocimetry and proper orthogonal decomposition analysis. *Physics*

- of Fluids, 31[2], 025101.
- Nield, D. A., & Bejan, A. [2017]. *Convection in Porous Media*, 5th edn, Springer International Publishing. doi:10.1007/978-3-319-49562-0
- Rao, F., & Jin, Y. [2022]. Possibility for survival of macroscopic turbulence in porous media with high porosity. *Journal of Fluid Mechanics*, 937, A17.
- Seguin, D., Montillet, A., Comiti, J., & Huet, F. [1998]. Experimental characterization of flow regimes in various porous media—II: Transition to turbulent regime. *Chemical Engineering Science*, 53[22], 3897–3909.
- Srikanth, V., Huang, C.-W., Su, T. S., & Kuznetsov, A. V. [2021]. Symmetry breaking of turbulent flow in porous media composed of periodically arranged solid obstacles. *Journal of Fluid Mechanics*, 929, A2.
- Uth, M. F., Jin, Y., Kuznetsov, A. V., & Herwig, H. [2016]. A direct numerical simulation study on the possibility of macroscopic turbulence in porous media: Effects of different solid matrix geometries, solid boundaries, and two porosity scales. *Physics of Fluids*, 28[6], 065101.
- Zhao, C. Y., & Lu, T. J. [2002]. Analysis of microchannel heat sinks for electronics cooling. *International Journal of Heat and Mass Transfer*, 45[24], 4857–4869.